Geophysical Research Letters

Supporting Information for

Likely P-to-S Conversion at the Core-mantle Boundary Extracted from Array Processing of Noise Records

Tianze Liu[1], Peter M. Shearer[1]

[1]Institute of Geophysics and Planetary Physics, Scripps Institution of Oceanography, UC San Diego

Contents of this file

Supplementary Text 1

Effects of 3D velocity structure on *PKP* slowness

We performed beamforming using the same dataset for four earthquakes from the USGS earthquake catalog (EQ1–4) close to one of our *PKP* sources with slowness > 0.032 s km^{-1} (2013-07-06-00-00-00; Fig. S1). Among them, EQ1 and EQ2 show good agreement between the observed slownesses and the one predicted using IASP91, whereas EQ3 and EQ4 show greater slownesses than the 1D predictions (Fig. S1c), which is probably due to lateral heterogeneity along the ray paths. We thus infer that our *PKP* beams with slowness > 0.032 s km^{-1} may actually represent *PKPbc* waves whose slownesses are elevated due to similar 3D structural effects. We note that 3D structural effects likely also cause errors in our *PKP* source locations, which should only be regarded as preliminary estimates.

Supplementary Text 2

Spatial distribution of our *PKP* sources

To derive the approximate source locations for the time windows that are dominated by *PKP* energy from a single direction and are less likely affected by earthquake late coda, we convert their high-resolution *PKP* slowness vectors to source locations using the *PKP* slowness-distance relation computed with the IASP91 earth model (Kennett et al., 1995). When different time windows have the same *PKP* slowness vector, we regard them as having the same source locations and record their cumulative duration (number of hours; Fig. S2), which is sufficient for a preliminary characterization of these sources. We note that these estimated source locations are only approximate, as the slowness peaks are relatively broad in our images, 3D heterogeneity likely introduces deviations between observed slownesses and those predicted by 1D models, and the ocean-wave sources themselves are spatially defused rather than concentrated like earthquakes. A more detailed study of the spatial extent and temporal evolution of these sources will require back-projection imaging using data collected by arrays with a larger aperture than used here, which is beyond the scope of this study.

Our *PKP* sources are predominantly located in the Southern Ocean, where the ocean waves are the highest among all water bodies in the *PKP* range of our array (Fig. S2a). We also observe far more *PKP* sources in the southern winter (Jul 2012–Sep 2012 and Apr 2013–Sep 2013) than in the southern summer (Oct 2012–Mar 2013) of our observation period (Fig. S2a), which is likely due to the greater wave height in the Southern Ocean in winter. In addition to wave height, a proxy for wave energy, P-wave radiation of ocean-solid-earth interactions is also controlled by wave period and ocean depth, which can be characterized using the ocean site effect (Gualtieri et al., 2014). Our *PKP* sources appear to be mostly located in areas with high ocean P-wave site effect at 4 and 5 s. The correlations between the spatial distribution of our *PKP* sources and the wave height and the ocean-site effect indicate that our *PKP* waves likely result from the nonlinear interaction of ocean gravity waves generated by storms (Gualtieri et al., 2014).

Supplementary Text 3

Difference between stacking before and after cross-correlation

We denote the frequency-domain vertical-component and one of the horizontal-component records of stations 1–*N* as $V_1, V_2 \cdots V_N$ and $H_1, H_2 \cdots H_N$, respectively. Therefore, the frequency-domain vertical-horizontal cross-correlation function computed by stacking the cross-correlation functions of individual stations is

$$X = \sum_{i=1}^{N} V_i H_i^*$$

In which $*$ denotes complex conjugation. In contrast, the frequency-domain vertical-horizontal cross-correlation function computed by stacking the records from individual stations ("array stacking") before performing cross-correlation is

$$\tilde{X} = \left(\sum_{i=1}^{N} V_i\right)\left(\sum_{i=1}^{N} H_i^*\right)$$
$$= \sum_{i=1}^{N} V_i H_i^* + \sum_{i=1}^{N}\left(V_i \sum_{j=1,\ j\neq i}^{N} H_j^*\right)$$

Which clearly shows that the results with and without array stacking are different by the sum of the cross terms between different stations.

Supplementary Text 4

Estimating the splitting parameters from *PKS-PKP* waveforms

We used the covariance-matrix method (e.g., Shearer, 2019) to derive the fast direction and split time from our *PKS-PKP* observations. For each combination of fast direction and split time, we project the observed east- and north-component *PKS-PKP* records onto the fast and slow axes. We then correct for the split time by delaying the fast component by the split time. We finally compute the waveform covariance matrix with the corrected fast- and slow-component records and derive its two eigenvalues λ_1 and λ_2, with $\lambda_1 > \lambda_2$. A greater ratio between λ_1 and λ_2 indicates a particle motion closer to linear. We thus compute the eigenvalue ratios for grid points with fast direction in 0–180° and split time in 0–3 s and find the combination that maximizes the ratio, which gives the optimum fast direction and split time (Figs. 5 and S4c).

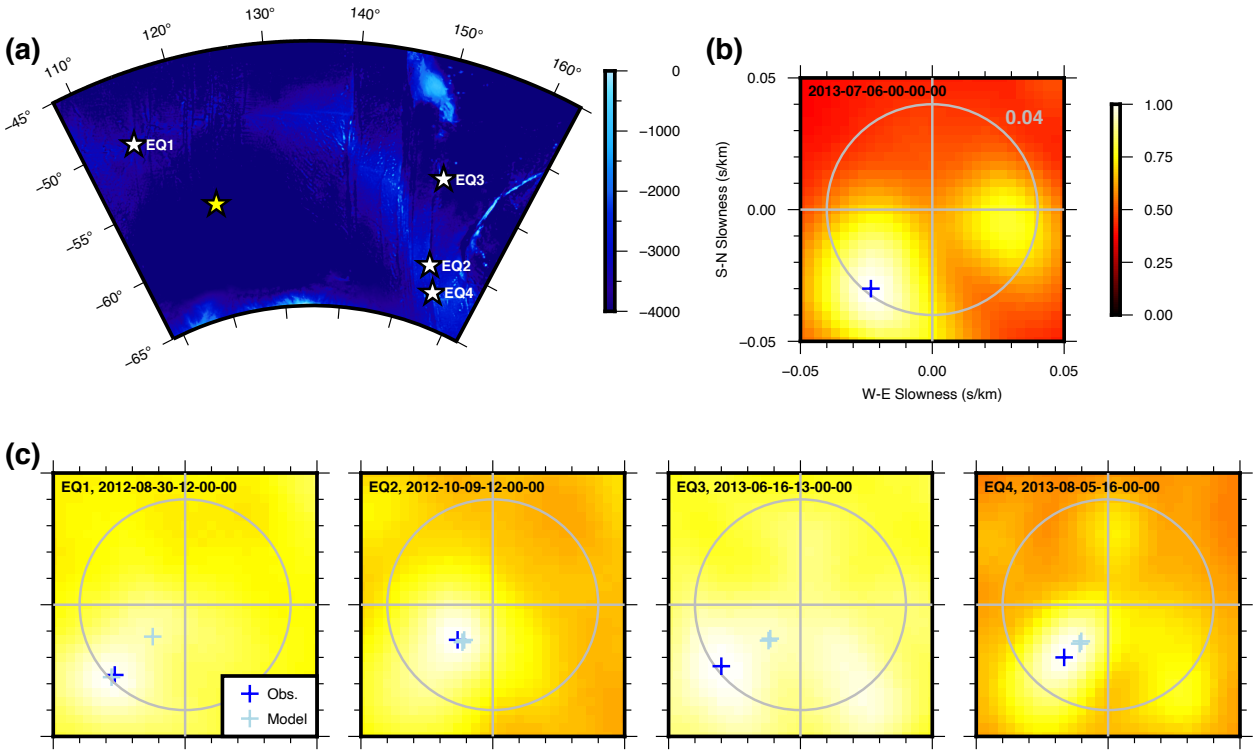

Figure S1. Using earthquakes with known locations to evaluate biases in our beamforming. (a) Locations of Earthquake (EQ) 1–4 used for calibration (white stars) and the derived *PKP*-source location of time window 2013-07-06-00-00-00 (yellow star). (b) Slowness image of the time window 2013-07-06-00-00-00 with the maximum marked with a dark blue cross. The gray circle denotes the slowness of 0.04 s km^{-1}. (c) Same as (b), but for EQ 1–4. The light blue crosses mark the slowness vectors predicted with IASP91 (multiple slownesses are due to different PKP branches).

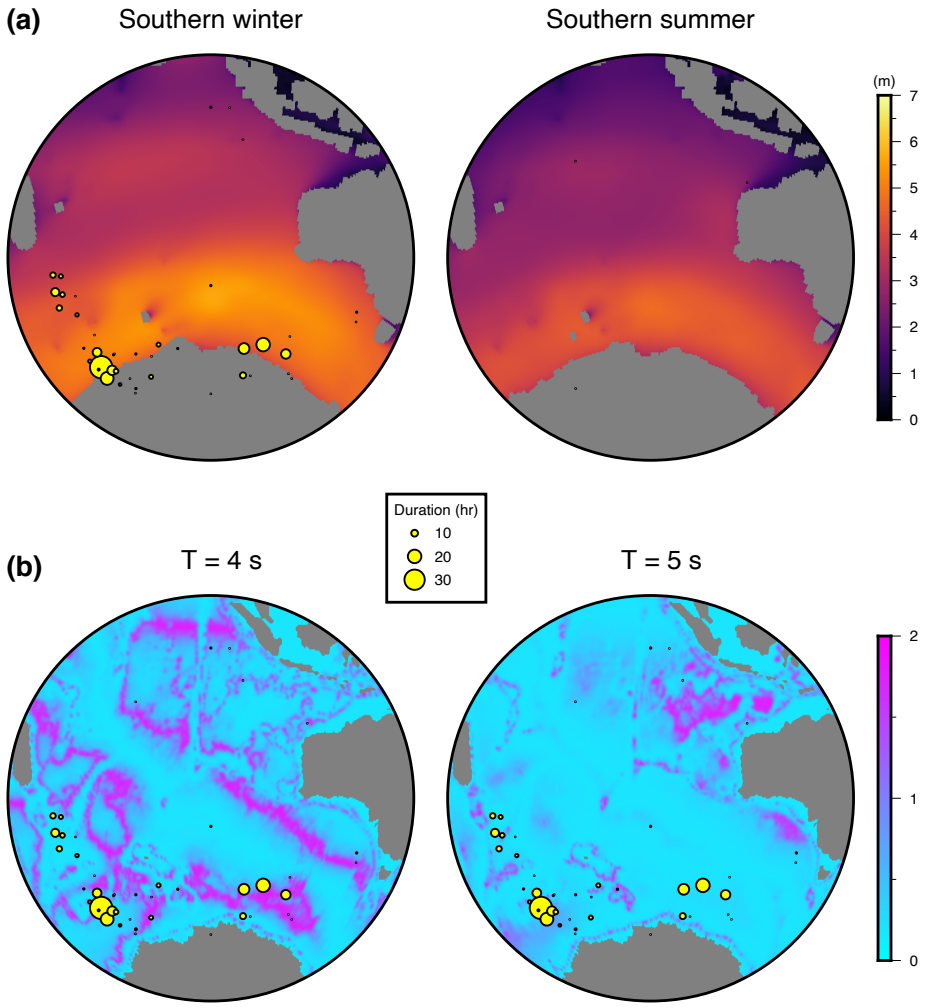

Figure S2. *PKP* source locations of our *PKP* windows that are less likely affected by earthquake late coda**.** Circle size denotes the cumulative duration of a certain location. (a) Sources in southern winter (left) and southern summer (right) plotted on the average significant wave-height maps of the corresponding seasons from WAVEWATCH III. (b) Sources plotted on the ocean P-wave site-effect maps at 4-s and 5-s periods from Gualtieri, et al., 2014.

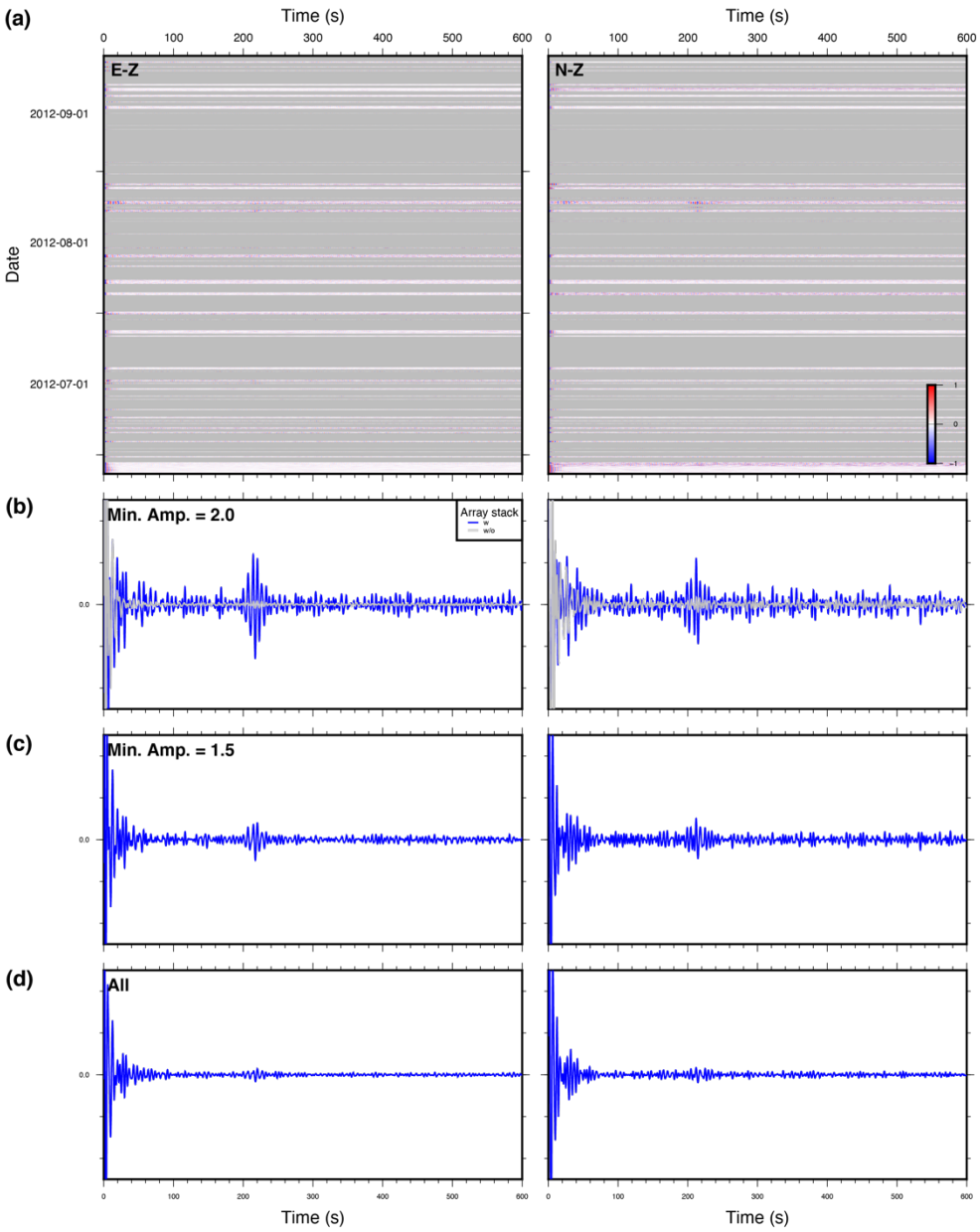

Figure S3. The same as Fig. 3 but computed using only the time windows less affected by global-earthquake late coda. The temporal variations of *PKP*-beam and 215-second-phase amplitude are not plotted because the curves are extremely fragmentated due to the removal of most of the time windows.

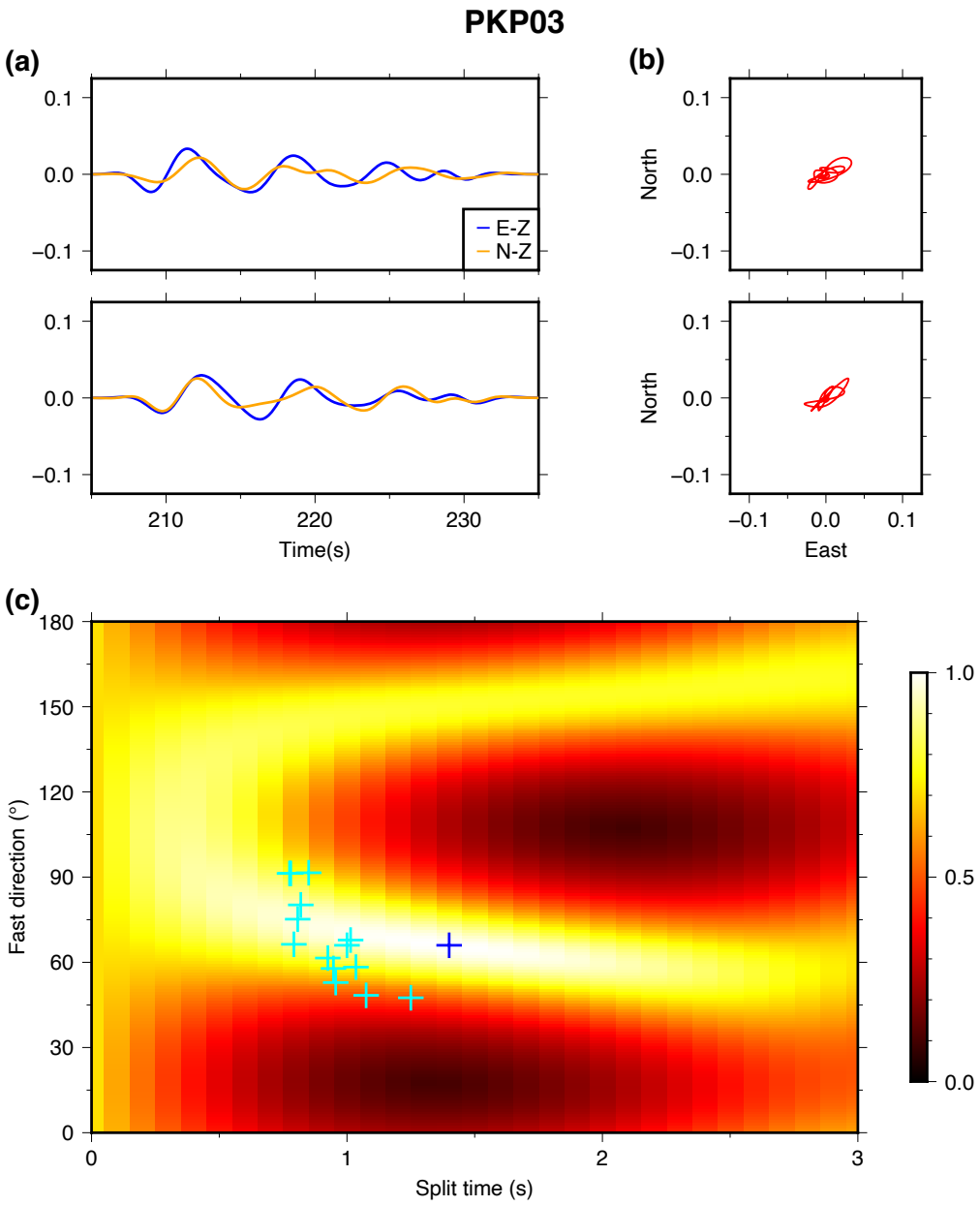

Figure S4. Same as Fig. 5, but for the source bin PKP03.

Reference:

Gualtieri, L., Stutzmann, E., Farra, V., Capdeville, Y., Schimmel, M., Ardhuin, F., & Morelli, A. (2014). Modelling the ocean site effect on seismic noise body waves. Geophysical Journal International, 197(2), 1096–1106. https://doi.org/10.1093/gji/ggu042

Kennett, B. L. N., Engdahl, E. R., & Buland, R. (1995). Constraints on seismic velocities in the Earth from traveltimes. Geophysical Journal International, 122(1), 108–124. https://doi.org/10.1111/j.1365-246X.1995.tb03540.x

Shearer, P. M. (2019). Introduction to Seismology (3rd ed., pp. 339–343 for shear-wave splitting section). Cambridge University Press. https://doi.org/10.1017/9781316877111